Three-Dimensional Structure of the Respiratory Chain Supercomplex $I_1III_2IV_1$ from Bovine Heart Mitochondria[†,‡]

Eva Schäfer,*[,§,||] Norbert A. Dencher,*[,§] Janet Vonck,[⊥] and David N. Parcej[⊥,▽]

Physical Biochemistry, Department of Chemistry, Petersenstrasse 22, Darmstadt University of Technology, D-64287 Darmstadt, and Department of Structural Biology, Max-Planck-Institute of Biophysics, Max-von-Laue-Strasse 3, D-60438 Frankfurt am Main, Germany

Received May 22, 2007; Revised Manuscript Received August 29, 2007

ABSTRACT: The respiratory chain complexes can arrange into multienzyme assemblies, so-called supercomplexes. We present the first 3D map of a respiratory chain supercomplex. It was determined by random conical tilt electron microscopy analysis of a bovine supercomplex consisting of complex I, dimeric complex III, and complex IV ($I_1III_2IV_1$). Within this 3D map the positions and orientations of all the individual complexes in the supercomplex were determined unambiguously. Furthermore, the ubiquinone and cytochrome *c* binding sites of each complex in the supercomplex could be located. The mobile electron carrier binding site of each complex was found to be in proximity to the binding site of the succeeding complex in the respiratory chain. This provides structural evidence for direct substrate channeling in the supercomplex assembly with short diffusion distances for the mobile electron carriers.

In mammals, most energy in the cell is produced by processes which take place within the respiratory chain. The respiratory chain comprises a number of membrane-bound enzyme complexes which transfer electrons from NADH to oxygen to ultimately produce water and generate a transmembrane proton gradient. Initially, the electrons from NADH are transferred via complex I (NADH:ubiquinone oxidoreductase) and ubiquinone to complex III (ubiquinol: cytochrome *c* oxidoreductase). Thereafter they pass through the peripheral electron carrier cytochrome *c* and complex IV (cytochrome *c* oxidase) to the terminal acceptor, molecular oxygen. The electrochemical proton gradient generated is used by complex V (F_OF_1-ATP synthase) to produce ATP.

In the past decade, structures of the individual respiratory chain complexes from various organisms have been determined. In the case of bovine heart mitochondria there exist atomic models of complex III (*1*−*5*) and complex IV (*6*−*8*), and electron microscopy 3D maps have been calculated for complex I (*9*).

In many organisms these complexes are assembled into supercomplexes. Such an arrangement may increase the electron-transfer rate by ensuring that the individual complexes and mobile electron carriers (ubiquinone and cytochrome *c*) are in close proximity (*10*). In addition, the organization into a supercomplex leads to an improved stabilization of the individual complexes (*11*−*16*). Respiratory supercomplexes of different compositions have been found in bacteria, e.g., *Paracoccus denitrificans* (*15*), in mitochondria from *Saccharomyces cerevisiae* (*17*, *18*), other fungi (*12*), higher plants (*19*−*21*), and mammals (*14*, *18*, *22*, *23*) by means of colorless and blue native polyacrylamide gel electrophoresis (BN-PAGE),[1] gel filtration, and immunoprecipitation. However, little is known about the architecture of these multicomplex assemblies. 2D projection maps of a supercomplex consisting of monomeric complex I and dimeric complex III (I_1III_2) from the plant *Arabidopsis thaliana* (*24*), a supercomplex consisting of a complex III dimer and two copies of complex IV (III_2IV_2) from yeast (*25*) and of the two supercomplexes I_1III_2 and $I_1III_2IV_1$ from bovine heart mitochondria (*16*) were obtained by electron microscopy. However, it was not possible to determine the arrangement of most of the individual complexes in the 2D projections.

To determine the positions and interactions of the complexes in such an assembly, we calculated a 3D map of supercomplex $I_1III_2IV_1$ from bovine heart mitochondria. The 3D structure is the first to be determined for a respiratory supercomplex. In the 3D map the positions and orientations of all complexes in the supercomplex were determined unambiguously. The putative mobile electron carrier (ubiquinone or cytochrome *c*) binding site of each complex is facing the corresponding binding site of the succeeding complex in the respiratory chain. In this assembly both electron

[†] This work was supported by the Deutsche Forschungsgemeinschaft (Grant SFB 472 to N.A.D./H. Seelert and W. Kühlbrandt) and by Grant ECFP6 (MiMage, to N.A.D.).

[‡] The EM 3D map has been deposited at the EM database (http://www.ebi.ac.uk/msd/index.html) with the accession number EMD-1318.

* To whom correspondence should be addressed. E-mail: e.schaefer@mail.cryst.bbk.ac.uk. Phone: +44 (0)20 7631 6835. Fax: +44 (0)20 7631 6803. E-mail: nad@pop.tu-darmstadt.de. Phone: +49 (0)6151 16527. Fax: +49 (0)6151 164171.

[§] Darmstadt University of Technology.

[||] Present address: School of Crystallography, Birkbeck College, University of London, Malet St., London WC1E 7HX, U.K.

[⊥] Max-Planck-Institute of Biophysics.

[▽] Present address: Institute of Biochemistry, Biocenter, Johann Wolfgang Goethe-University, Frankfurt am Main, Max-von-Laue-Strasse 9, D-60438 Frankfurt, Germany.

[1] Abbreviation: BN-PAGE, blue native polyacrylamide gel electrophoresis.

10.1021/bi700983h CCC: $37.00
Published on Web 10/10/2007

carriers have short diffusion distances, supporting the notion of a more efficient electron transfer along the respiratory chain when the complexes are associated within a supercomplex.

MATERIALS AND METHODS

Sample Preparation. Supercomplex $I_1III_2IV_1$ was isolated in its active state from bovine heart mitochondria according to ref *16*. The supercomplex sample with a concentration of ~0.4 mg/mL was stored in 0.1% (w/v) digitonin, 25 mM tricine, 7.5 mM bis-tris, 25 mM ϵ-aminocaproic acid, 10% (w/v) glycerol, pH 7.1, at −80 °C.

Transmission Electron Microscopy. The undiluted supercomplex $I_1III_2IV_1$ sample was negatively stained with 2% (w/v) ammonium molybdate according to the deep stain method (*26*) to ensure that the whole supercomplex was embedded in stain, which was not possible with uranyl acetate stained samples. Electron micrographs were recorded on Kodak SO-163 electron image film using a Philips CM120 at 120 kV under low dose conditions, at a magnification of 45000×. Tilt pairs were collected with the first micrograph at a nominal tilt angle of 50° and the second, of the same area, at 0°. A defocus of ~1500 nm on the tilt axis for the tilted micrograph and ~700 nm for the untilted micrograph was employed. Micrographs were digitized on a PhotoScan scanner (Z/I Imaging, Aalen, Germany) at a pixel size of 7 μm, corresponding to 1.56 Å on the specimen. Subsequently, adjacent pixels were averaged to yield a pixel size of 4.67 Å.

Image Processing and 3D Reconstruction. Top-view images were processed using SPIDER (System for Processing Image Data in Electron microscopy and Related fields, version 5, with modifications) (*27*). The 3D reconstruction was preformed by the random conical tilt method (*28*), using scripts written by M. Radermacher and D. Parcej (Max-Planck-Institute of Biophysics, Germany). Equivalent particles from tilted- and untilted-view images were identified and selected using the "tilted particles" option in WEB (*27*). This enabled determination of the tilt geometry (tilt axis direction and tilt angle) for each micrograph. Afterward, the particles were windowed into 128 × 128 pixel boxes. To avoid reference bias, images from the zero-degree micrograph were centered against a circular mask, and a first average was calculated using reference-free alignment (*29*). This average was then used as the initial reference for three rounds of direct translational and rotational alignment. The top views were subjected to a neuronal network analysis implemented in XMIPP (X-windows based Microscopy Image Processing Package; *30*). Three nodes from the resulting map were selected and used as references for multireference alignment using Radon transforms (*31*). This yielded three classes. The tilted-view images were filtered to 3.0 nm. This value was chosen such that all tilted 2D images were truncated to a resolution lower than the first zero of the theoretical contrast transfer function for the particle (calculated using the nominal defocus and tilt parameters). This was done because we were unable to detect Thon rings due to the thickness of the stain layer and thus could not determine the defocus of the tilted micrographs. Then the tilted-view images were centered against the equivalent, aligned zero-degree images and grouped in classes on the basis of the classification of the zero-degree images. 3D maps were then calculated for each of the classes from Radon transforms of the tilted-view images (*32*).

Visually similar 3D maps with values of the cross-correlation coefficients with each other higher than 0.94 were combined by aligning the tilted-view images from the appropriate classes to the Fourier-transformed Radon transform of one of the 3D maps to be combined (*31*). The combined 3D map was refined twice by aligning in a similar manner. After refinement, the resolution of the final 3D map was determined by Fourier shell correlation (*33*, *34*) with a cutoff of 3 times the noise correlation or the 0.5 FSC criterion. For further studies the map was filtered to 3.6 nm with a Fermi low-pass filter. The molecular mass of the 3D map was calculated with a coefficient of 1.37 g/cm^3. An elongation factor of 1.4 was calculated due to the missing cone.

Fitting of the Individual Complexes in the Supercomplex 3D Map. A negative stain 3D map of bovine complex I filtered to 5.0 nm was supplied by N. Grigorieff (*9*). The X-ray structures of bovine complex III (PDB ID 2A06, *4*) and complex IV (PDB ID 1OCC, *6*) were used for fitting of the complex III dimer and complex IV monomer. Fitting of the individual complexes (I, III_2, and IV) was performed by hand in Chimera (*35*; UCSF Chimera package of the Resource for Biocomputing, Visualization & Informatics, University of California, San Francisco, supported by NIH Grant P41 RR-01081).

RESULTS AND DISCUSSION

Recently, we showed that it was possible to isolate active bovine heart supercomplex $I_1III_2IV_1$ from mitochondrial membranes solubilized in digitonin using BN-PAGE and electroelution (*16*). 2D projection class averages obtained by single-particle electron microscopic analysis showed that the protein favored distinct orientations on the carbon support film of specimens stained with uranyl acetate (*16*): "top" views as looking perpendicular to the membrane surface and "side" views as looking along the membrane plane.

In our previous study (*16*) a 3D map of the supercomplex was not generated. Subsequent attempts to obtain higher resolution data by embedding the supercomplex in ice were unsuccessful due to the low concentration of protein that could be achieved. Approaches to reach a higher concentration during or after purification failed because the supercomplex aggregated irreversibly at concentrations higher than ~0.5 mg/mL. We therefore decided to calculate a three-dimensional map of the supercomplex embedded in a deep ammonium molybdate stain.

The distinct orientations described in our previous study (*16*) were also observed here for the ammonium molybdate stained protein (Figure 1A,B), showing that the type of stain used had no major effect on the shape of the protein. The side views are roughly L-shaped, while the top views are triangular with the three sides all of different lengths.

Because of the distinct orientations of the particles on the carbon support, we decided to use a tilt-pair data collection strategy (random conical tilt) (*28*). In this scheme, a micrograph of the specimen is taken in a highly tilted orientation (e.g., ~50°), followed by an image of the same specimen area with zero tilt. From the untilted micrograph

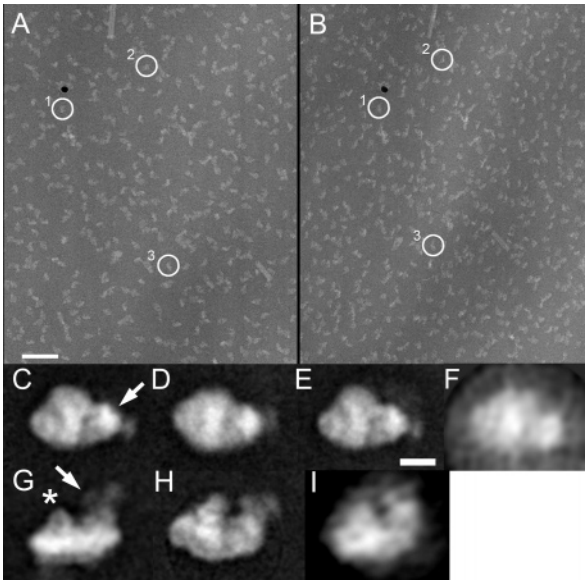

FIGURE 1: Transmission electron microscopy of supercomplex $I_1III_2IV_1$ particles and resulting class averages. Tilt pair of a grid area in the **(**A**)** untilted (0°) position and in the **(**B**)** 50° tilted position. In each micrograph the same three particles are marked with circles. Particles 1 and 3 are side views, and particle 2 is a top view. The long particle in the upper left of the electron micrographs is tobacco mosaic virus (TMV), and the black spot above particle 1 is a colloidal gold particle (∅ = 20 nm). Both were used for orientation and locating the same grid area in the untilted and tilted micrographs. Class averages of top views obtained from multireference alignment: (C) average of 593 particles, (D) average of 430 particles, and (E) average of 482 particles. (F) Reprojection of the final 3D map along the *z*-axis to represent a top-view orientation. Class averages of side views obtained from multireference alignment: (G) average of 236 particles and (H) average of 201 particles. (I) Reprojection of the final 3D map to represent a side-view orientation. The matrix arm of complex I, which is the stain-excluding density in the top views, is labeled with a white arrow in (C) and (G). The matrix domains of complex III_2 are labeled with an asterisk in (G). The scale bars represent (A) 100 nm and (C−I) 10 nm.

the particle images are aligned and classified to identify particles with the same orientation on the carbon. Since the particles are randomly oriented in the plane of the carbon film, the images in the tilted micrograph exhibit a random conical geometry (*28*). From the tilt angle and the relative rotation in the plane, two of the Euler angles required for the reconstruction are known. The third is assumed to be the same for all particles which display the same view in the zero-tilt images. The three derived Euler angles are applied to the tilted-view images, and 3D maps are calculated by weighted back-projection. 3D maps are calculated for each individual class, and similar maps are then combined.

From 20 tilt pairs 2183 particles were selected. The majority (80%) of the particles displayed top views, whereas only the minority (20%) had side-view orientations. Hence, the distribution between top and side views is the same as in uranyl acetate stained bovine supercomplex samples (*16*).

The top-view particles were separated into three main classes. All of the top views (Figure 1C−E) showed a bright, stain-excluding density (marked with a white arrow in Figure 1C), which was identified as the matrix arm of complex I (*16*). Two of the top-view class averages showed the characteristic triangular shape (Figure 1C,E), whereas the third top view displayed a more oval shape (Figure 1D). The different appearance of this top view is probably due to an orientation on the carbon support film slightly different from those of the other two classes. Side-view particles were separated into two main classes (Figure 1G,H). The matrix arm of complex I (marked with a white arrow in Figure 1G) and the matrix domains of complex III_2 (marked with an asterisk in Figure 1G), which have been identified in our earlier study (*16*), are clearly visible. Because of their low occurrence side views were not subjected to any further analysis.

3D maps of the top views were calculated corresponding to the three class averages (Figure 1C−E). The 3D maps of two classes (Figure 1C,D) were visually identical and so were combined. The 3D map from Figure 1E showed a different orientation in its distal domains and was not included. After refinement, the resulting map (Figure 2, left column) was found to have a resolution of 3.2 and 3.9 nm as determined by Fourier shell correlation according to the 3σ criterion or the 0.5 cutoff criterion (*33*, *34*), respectively. Importantly, when the final 3D map was reprojected along the *z*-axis representing a top-view orientation (Figure 1F) and also reprojected to present a side-view orientation (Figure 1I), the resulting images were consistent with the untilted class averages (Figure 1C−E,G), showing that the 3D map is a valid representation of the data.

The higher protrusion seen in a side view of the 3D map (Figure 2, left column) has a total height of 17 nm and the smaller one a height of 14 nm. The membrane integral part of the supercomplex has dimensions of 20 × 15 nm. The final 3D map was displayed at a threshold of 2σ and has a calculated molecular mass of 1700 kDa, which corresponds very well to the experimentally determined mass (*16*) of the whole supercomplex including residual bound detergent, lipid, and Coomassie. Hence, it can be concluded that the supercomplex particles are completely embedded in the ammonium molybdate stain.

Positions of the Individual Complexes in Supercomplex $I_1III_2IV_1$. The X-ray structures of complexes III_2 (*4*) and IV (*6*) as well as a negative stain 3D map of complex I (*9*) were fitted in the 3D map. In this way it was possible to locate all three individual complexes unambiguously (Figure 2). The highest protrusion in the map represents the matrix arm of complex I. The position of complex IV was determined in our previous study (*16*) at the opposite end of the supercomplex and confirmed by our 3D map. The smaller protrusion embodies the matrix domains of complex III_2. The remaining density was assigned to the membrane arm of complex I, fixing the orientation of complex I.

The higher protrusion in the side view (Figure 2) represents the matrix arm of complex I (Figure 2, middle and right columns). The individual complex I (marked yellow in Figure 2, middle and right columns) displays the same angle between the matrix and the membrane arm as complex I in the supercomplex (Figure 2). The distal matrix domains in the supercomplex are bent toward the membrane domains and have a slightly different shape compared to the isolated complex I. This results in the matrix arm protruding from the supercomplex 3D map when complex I is fitted.

The functionality of complex I in the supercomplex was shown by the in-gel NADH dehydrogenase activity of the matrix arm as well as spectrometric NADH:ubiquinone oxidoreductase activity of the whole complex (*16*). Further-

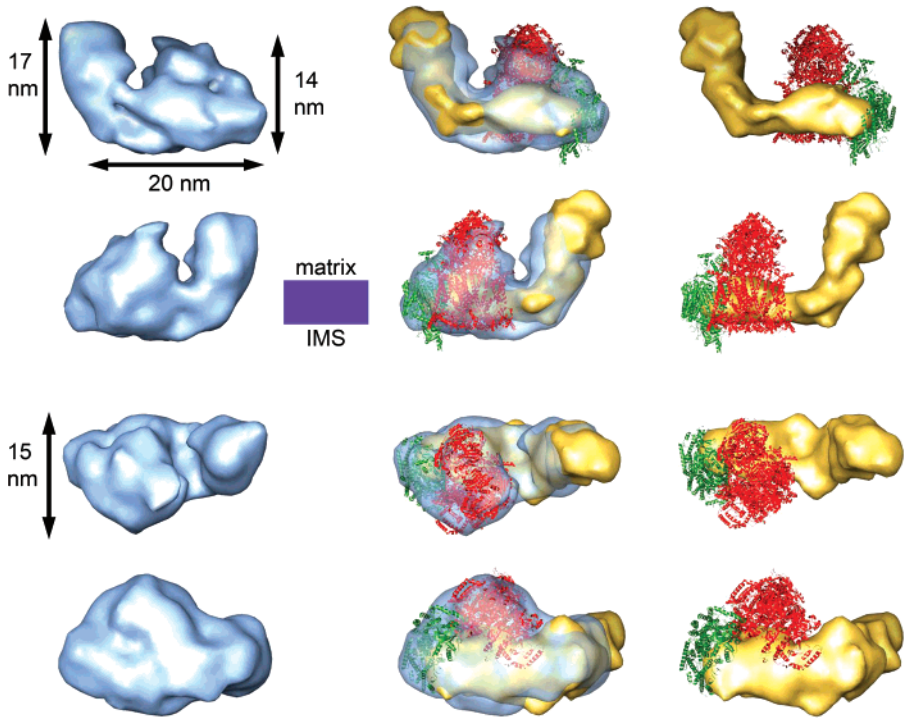

FIGURE 2: Comparison of the 3D map of supercomplex $I_1III_2IV_1$ with those of the individual complexes. The left column shows a surface representation in blue of the supercomplex $I_1III_2IV_1$ 3D map. The middle column displays the 3D map with a semitransparent surface and the fitted structures of the individual complexes. The right column shows only the three individual complexes as they would assemble to form the supercomplex. The two upper rows display side views along the membrane plane. The third row shows the particles as seen from the matrix space and the lower row as seen from the intermembrane space. The electron microscopic 3D map of complex I filtered to 5.0 nm (*9*) is shown in yellow, the X-ray structure of complex III_2 (PDB ID 2A06, *4*) is displayed in red, and the X-ray structure of complex IV (PDB ID 1OCC, *6*) is shown in green. The location of the membrane in a side view is displayed in purple. IMS = intermembrane space.

more, the matrix arm subunits 24, 49, 51, and 75 kDa were identified by MALDI peptide mass fingerprinting (*16*). All iron−sulfur clusters required for electron transfer are located in the matrix arm, and the NADH binding site is located in the matrix arm subunit 51 kDa (*36*). Taking these data together, it can be ruled out that the difference in appearance of the matrix arm in the individual complex I and complex I in the supercomplex is caused by a loss of complex I subunits in the supercomplex.

On the carbon support film the individual complex I particles favor side-view orientations (*9*), whereas the supercomplex particles favor top-view orientations. Hence, the different shapes of the matrix arm and the protrusion of individual complex I may be caused by the negative stain and by different interactions with the carbon support film of the individual complex I and the supercomplex $I_1III_2IV_1$. The matrix domains of complex I could be distorted in another way than in the 3D map of the individual complex I, or the different shape could be due to a slight twist of the matrix domains in the supercomplex. The matrix arm of complex I shows a variability in the conformation of its domains (*37*); thus, the structural differences of the matrix arm of the individual complex I and complex I in the supercomplex could also be due to different conformations.

Recently, the structure of the soluble arm of complex I from *Thermus thermophilus* has been determined by X-ray crystallography (*36*). We attempted to fit the structure of the soluble arm in our supercomplex, but as complex I from bovine heart mitochondria contains a number of "accessory" subunits in comparison to that from *T. thermophilus*, it is not possible to compare the two structures directly with each other, and an unambiguous fit was not feasible. The ubiquinone binding site of complex I is believed to be in the peripheral matrix arm close to the connection of the matrix arm and the membrane arm (*36*, *38*−*40*). The subunits 49 kDa and PSST seem to play a major role in this binding pocket (*38*, *39*).

The smaller protrusion (14 nm) in the side view of the 3D map of supercomplex $I_1III_2IV_1$ (Figure 2) corresponds to the matrix domains of the complex III dimer (*4*). The width of the membrane integral part of the supercomplex (15 nm) consists of the membrane parts of complexes I and III_2. One of the complex III monomers of the dimer is facing the lipid. The other one is attached to the membrane arm of complex I. As mentioned above, the quinone binding site in complex I is believed to be in the matrix arm (*36*, *38*, *39*, *40*) near the junction of the matrix and membrane arms. The ubiquinone binding site in complex III is located at the Rieske iron−sulfur protein and cytochrome *b* (*4*, *41*, *42*). On the basis of the structures of the individual complexes fitted into the supercomplex, these subunits seem to be attached to the complex I membrane arm close to its matrix−membrane arm connection and face the putative ubiquinone binding site in complex I. The ubiquinone coming from complex I reaches its binding site in the complex III dimer via a cavity which in our model is facing the proposed ubiquinone binding site in complex I (Figure 3).

In the supercomplex 3D map, the distal domains of core proteins I and II of complex III_2 appear to have a shape different from that in the X-ray structure. As a consequence, complex III_2 in the supercomplex has a height of 14 nm and not the 15 nm expected from the X-ray structure (*4*). For

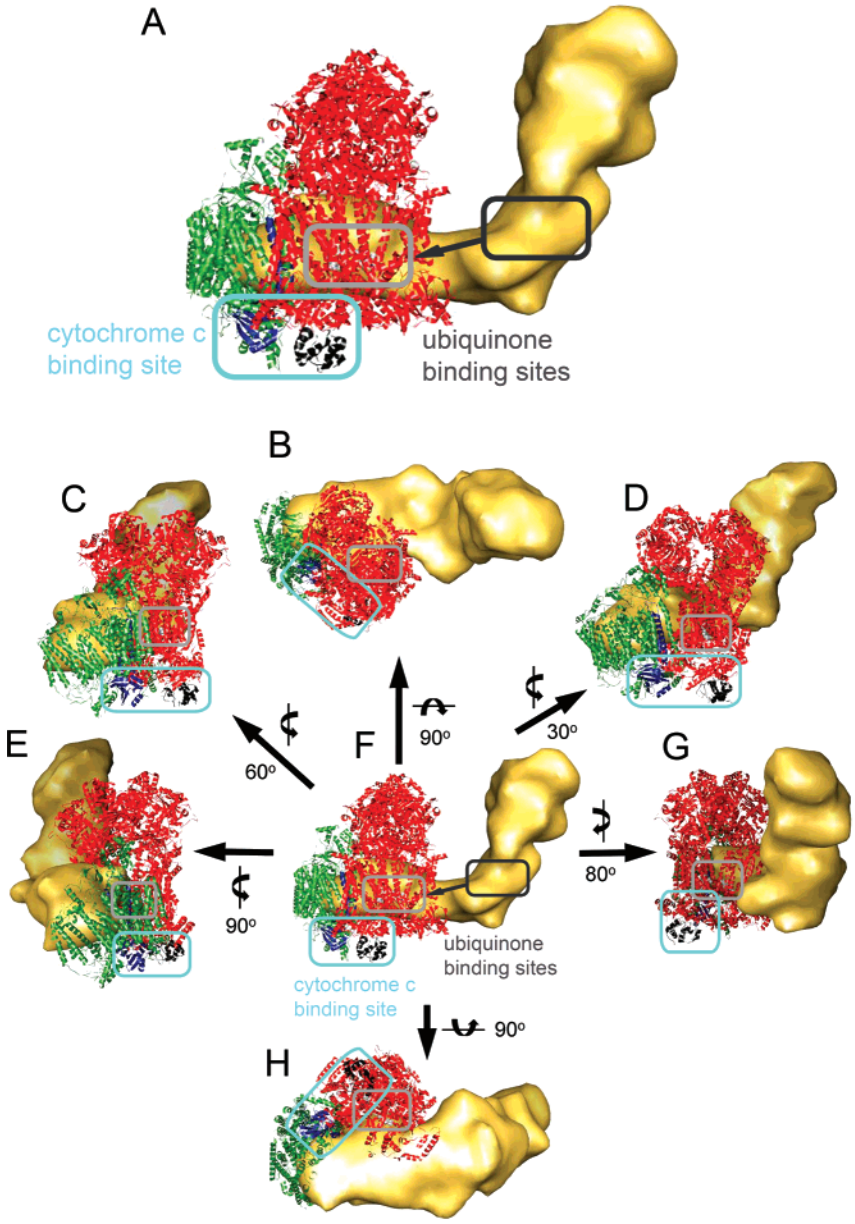

FIGURE 3: Electron carrier binding sites in the supercomplex. (A) Magnified side view along the membrane plane. (B) Top view from the matrix side. (C−G) Side views along the membrane plane. (H) Bottom view from the intermembrane space. The individual complexes in the supercomplex are shown in yellow (complex I), red (complex III_2), and green (complex IV). (A, F) The ubiquinone interaction site in complex I is marked in dark gray, and the interaction site in the complex III dimer is marked in gray. In all other representations only the ubiquinone interaction site in the complex III dimer is marked in gray. The two cytochrome b_L hemes of the complex III dimer, which are the ubiquinone interaction site, are shown in light gray. The ubiquinone diffuses from its interaction site in complex I to its interaction site in the complex III dimer, shown as a dark gray arrow in (A) and (F). The cytochrome *c* interaction site in complexes III and IV is marked in light blue in (A)−(H). Cytochrome *c* bound to complex III is colored in black (from 1KYO (PDB ID); *43*), and subunit II, which is the cytochrome *c* binding site, from complex IV is displayed in blue. The rotations to obtain the different views are shown next to the arrows.

this reason, parts of the distal complex III_2 subunits from the X-ray data extend out of the 3D map. This can be due to conformational changes or rather likely a slight distortion of the supercomplex by the stain or masking effects of the polar distal domains by the ammonium molybdate.

Furthermore, some small membrane peripheral parts of the 2.8 Å resolution X-ray structures of complexes III_2 (*4*) and IV (*6*) are not seen in the negative stain 3D map of the supercomplex. The 3D map was filtered to 3.6 nm; it is possible that these small domains may not be visible at this resolution.

Previously, we determined the location and orientation of complex IV in the supercomplex by a difference map between supercomplexes $I_1III_2IV_1$ and I_1III_2 (*16*). Its position at the end of the complex I membrane arm is clearly confirmed by the 3D map. Together complexes I and IV form the 20 nm long membrane integral part (Figure 2). The complex IV monomer interacts with complex I (Figure 2) through a site which is the dimer interface in the X-ray structure (*6*). The cytochrome *c* binding site in complex III is at the cytochrome c_1 subunit (*43*). In complex IV cytochrome *c* is known to interact with the globular domains

of subunit II (*6*), although various other subunits have also been reported to play a role in binding. In *S. cerevisiae* the interaction of the individual complexes in a supercomplex consisting of complexes III and IV is proposed to be at the subunits cytochrome *b* and c_1 from complex III with IV (*44*). The lipid cardiolipin is thought to glue the two complexes together (*44*, *45*). On the basis of the fitted structure, in our 3D map the cytochromes *b* and c_1 from complex III_2 seem to face subunit II. Hence, the cytochrome *c* binding sites of both complexes are facing each other (Figure 3).

The stoichiometry of the supercomplex of $I_1III_2IV_1$ was confirmed by structural and biochemical studies (*16*, *18*, *22*). The presence of a complex III dimer might be essential for the assembly or stability of complex I (*11*−*16*). In addition, functional as well as structural data suggest that complex III is only active as a dimer (*41*−*43*, *46*). Our previous study (*16*) showed that complex IV exists as an active monomer in the supercomplex. This was also shown in a recent study (*25*) for a yeast supercomplex consisting of dimeric complex III and two complex IV monomers bound to opposite ends. In contrast to the situation in yeast (*25*), complex IV in our supercomplex interacts with the rest of the supercomplex with the interface, which is the dimer interface in the X-ray structure (*6*). Our supercomplex 3D map clearly confirms the presence of just one copy of complex IV as well as its orientation. Thus, in mammals the dimerization of complex IV might play a structural role, competing with supercomplex formation using the same contact interface (*16*).

Detailed studies have shown the reliability of 3D maps derived from negatively stained samples (*26*, *47*, *48*). Our 3D map represents the right molecular mass of ~1700 kDa for the supercomplex $I_1III_2IV_1$. Complex I, III, nor IV has a large domain in the intermembrane space (*4*, *6*, *9*), which is consistent with the appearance of the supercomplex 3D map (Figure 2). All complexes could be assigned to the supercomplex $I_1III_2IV_1$ 3D map unambiguously (Figure 2), and all membrane domains of the individual complexes in our model are at the same height, like they are expected in a lipid layer embedded arrangement. Together these observations support the overall reliability of our supercomplex 3D map.

Our 3D map of $I_1III_2IV_1$ gives the first insight into the positions and interactions of the individual respiratory chain complexes when assembled into a supercomplex. One function of the assembly into a supercomplex is the stabilization of the individual complexes. As proposed earlier (*11*, *12*, *14*, *16*) complexes III and IV are needed for the stability of complex I. The 3D map of $I_1III_2IV_1$ indeed shows extensive interaction sites of both complexes III_2 and IV with complex I, which will keep it in a stable conformation.

In the 3D map of supercomplex $I_1III_2IV_1$, the mobile electron carrier (ubiquinone or cytochrome *c*) binding site of one complex is facing and is in proximity to the mobile electron carrier binding site of the succeeding complex of the respiratory chain. This arrangement is significant as it results in short diffusion distances for ubiquinone and cytochrome *c*, thus facilitating a more efficient electron transfer from complex I via complex III to complex IV as proposed in the solid-state model (*10*).

The positions and orientations of the individual complexes in the multienzyme assembly give further evidence for a direct substrate channeling in the supercomplex.

ACKNOWLEDGMENT

We thank Niko Grigorieff for making available the negative stain 3D density map of complex I, Deryck Mills for help with the electron microscopy, Remco Wouts for help with computing, Werner Kühlbrandt for support and discussions as well as critical reading of the manuscript, Nicole Reifschneider and Frank Krause for the supply of bovine heart mitochondria, and Frank Krause, Holger Seelert, and Helen Saibil for discussion and reading the manuscript.

REFERENCES

1. Xia, D., Yu, C. A., Kim, H., Xia, J. Z., Kachurin, A. M., Zhang, L., Yu, L., and Deisenhofer, J. (1997) Crystal structure of the cytochrome bc1 complex from bovine heart mitochondria, *Science 27*, 60−66.
2. Iwata, S., Lee, J. W., Okada, K., Lee, J. K., Iwata, M., Rasmussen, B., Link, T. A., Ramaswamy, S., and Jap, B. K. (1998) Complete structure of the 11-subunit bovine mitochondrial cytochrome bc1 complex, *Science 281*, 64−71.
3. Esser, L., Quinn, B., Li, Y. F., Zhang, M., Elberry, M., Yu, L., Yu, C. A., and Xia, D. (2004) Crystallographic studies of quinol oxidation site inhibitors: a modified classification of inhibitors for the cytochrome bc(1) complex, *J. Mol. Biol. 341*, 281−302.
4. Huang, L. S., Cobessi, D., Tung, E. Y., and Berry, E. A. (2005) Binding of the respiratory chain inhibitor antimycin to the mitochondrial bc1 complex: a new crystal structure reveals an altered intramolecular hydrogen-bonding pattern, *J. Mol. Biol. 351*, 573−597.
5. Esser, L., Gong, X., Yang, S., Yu, L., Yu, C. A., and Xia, D. (2006) Surface-modulated motion switch: capture and release of iron-sulfur protein in the cytochrome bc1 complex, *Proc. Natl. Acad. Sci. U.S.A. 103*, 13045−13050.
6. Tsukihara, T., Aoyama, H., Yamashita, E., Tomizaki, T., Yamaguchi, H., Shinzawa-Itoh, K., Nakashima, R., Yaono, R., and Yoshikawa, S. (1996) The whole structure of the 13-subunit oxidized cytochrome c oxidase at 2.8 A, *Science 272*, 1136−1144.
7. Yoshikawa, S., Shinzawa-Itoh, K., Nakashima, R., Yaono, R., Yamashita, E., Inoue, N., Yao, M., Fei, M. J., Libeu, C. P., Mizushima, T., Yamaguchi, H., Tomizaki, T., and Tsukihara, T. (1998) Redox-coupled crystal structural changes in bovine heart cytochrome c oxidase, *Science 280*, 1723−1729.
8. Tsukihara, T., Shimokata, K., Katayama, Y., Shimada, H., Muramoto, K., Aoyama, H., Mochizuki, M., Shinzawa-Itoh, K., Yamashita, E., Yao, M., Ishimura, Y., and Yoshikawa, S. (2003) The low-spin heme of cytochrome c oxidase as the driving element of the proton-pumping process, *Proc. Natl. Acad. Sci. U.S.A. 100*, 15304−15309.
9. Grigorieff, N. (1998) Three-dimensional structure of bovine NADH:ubiquinone oxidoreductase (complex I) at 22 A in ice, *J. Mol. Biol. 277*, 1033−1046.
10. Chance B., and Williams G R. (1955) Respiratory enzymes in oxidative phosphorylation. III. The steady state, *J. Biol. Chem. 217*, 409−427.
11. Acin-Perez, R., Bayona-Bafaluy, M. P., Fernandez-Silva, P., Moreno-Loshuertos, R., Perez-Martos, A., Bruno, C., Moraes, C. T., and Enriquez, J. A. (2004) Respiratory complex III is required to maintain complex I in mammalian mitochondria, *Mol. Cell 13*, 805−815.
12. Krause, F., Scheckhuber, C. Q., Werner, A., Rexroth, S., Reifschneider, N. H., Dencher, N. A., and Osiewacz, H. D. (2004) Supramolecular organization of cytochrome c oxidase- and alternative oxidase-dependent respiratory chains in the filamentous fungus *Podospora anserina*, *J. Biol. Chem. 279*, 26453−26461.
13. Schägger, H. (2002) Respiratory chain supercomplexes of mitochondria and bacteria, *Biochim. Biophys. Acta 1555*, 154−159.
14. Schägger, H., de Coo, R., Bauer, M. F., Hofmann, S., Godinot, C., and Brandt, U. (2004) Significance of respirasomes for the assembly/stability of human respiratory chain complex I, *J. Biol. Chem. 279*, 36349−36353.

15. Stroh, A., Anderka, O., Pfeiffer, K., Yagi, T., Finel, M., Ludwig, B., and Schägger, H. (2004) Assembly of respiratory complexes I, III, and IV into NADH oxidase supercomplex stabilizes complex I in *Paracoccus denitrificans*, *J. Biol. Chem. 279*, 5000−5007.
16. Schäfer, E., Seelert, H., Reifschneider, N. H., Krause, F., Dencher, N. A., and Vonck, J. (2006) Architecture of active mammalian respiratory chain supercomplexes, *J. Biol. Chem. 281*, 15370−15375.
17. Cruciat, C. M., Brunner, S., Baumann, F., Neupert, W., and Stuart, R. A. (2000) The cytochrome bc1 and cytochrome c oxidase complexes associate to form a single supracomplex in yeast mitochondria, *J. Biol. Chem. 275*, 18093−18098.
18. Schägger, H., and Pfeiffer, K. (2000) Supercomplexes in the respiratory chains of yeast and mammalian mitochondria, *EMBO J. 19*, 1777−1783.
19. Eubel, H., Heinemeyer, J., and Braun, H. P. (2004) Identification and characterization of respirasomes in potato mitochondria, *Plant Physiol. 134*, 1450−1459.
20. Eubel, H., Jänsch, L., and Braun, H. P. (2003) New insights into the respiratory chain of plant mitochondria. Supercomplexes and a unique composition of complex II, *Plant Physiol. 133*, 274- 286.
21. Krause, F., Reifschneider, N. H., Vocke, D., Seelert, H., Rexroth, S., and Dencher, N. A. (2004) "Respirasome"-like supercomplexes in green leaf mitochondria of spinach, *J. Biol. Chem. 279*, 48369−48375.
22. Krause, F., Reifschneider, N. H., Goto, S., and Dencher, N. A. (2005) Active oligomeric ATP synthases in mammalian mitochondria, *Biochem. Biophys. Res. Commun. 329*, 583−590.
23. Reifschneider, N. H., Goto, S., Nakamoto, H., Takahashi, R., Sugawa, M., Dencher, N. A., and Krause, F. (2006) Defining the mitochondrial proteomes from five rat organs in a physiologically significant context using 2D blue-native/SDS-PAGE, J. *Proteome Res. 5*, 1117−1132.
24. Dudkina, N. V., Eubel, H., Keegstra, W., Boekema, E. J., and Braun, H. P. (2005) Structure of a mitochondrial supercomplex formed by respiratory-chain complexes I and III, *Proc. Natl. Acad. Sci. U.S.A. 102*, 3225−3229.
25. Heinemeyer, J., Braun, H.-P., Boekema, E. J., and Kouril, R. (2007) A Structural Model of the Cytochrome *c* Reductase/ Oxidase Supercomplex from Yeast Mitochondria, *J. Biol. Chem. 282*, 12240−12248.
26. Stoops, J. K., Schroeter, J. P., Bretaudiere, J. P., Olson, N. H., Baker, T. S., and Strickland, D. K. (1991) Structural studies of human alpha 2-macroglobulin: concordance between projected views obtained by negative-stain and cryoelectron microscopy, *J. Struct. Biol. 106*, 172−178.
27. Frank, J., Radermacher, M., Penczek, P., Zhu, J., Li, Y., Ladjadj, M., and Leith, A. (1996) SPIDER and WEB: processing and visualization of images in 3D electron microscopy and related fields, *J. Struct. Biol. 116*, 190−199.
28. Radermacher, M., Wagenknecht, T., Verschoor, A., and Frank, J. (1987) Three-dimensional reconstruction from a single-exposure, random conical tilt series applied to the 50S ribosomal subunit of *Escherichia coli*, *J. Microsc. 146*, 113−136.
29. Marco, S., Chagoyen, M., de la Fraga, L. G., Carazo, J. M., and Carrascosa, J. L. (1996) A variant to the "random approximation" of the reference-free alignment algorithm, *Ultramicroscopy 66*, 5−10.
30. Marabini, R., Masegosa, I. M., San Martin, M. C., Marco, S., Fernandez, J. J., de la Fraga, L. G., Vaquerizo, C., and Carazo, J. M. (1996) Xmipp: An image processing package for electron microscopy, *J. Struct. Biol. 116*, 237−240.
31. Radermacher, M., Ruiz, T., Wieczorek, H., and Gruber, G. (2001) The structure of the V(1)-ATPase determined by three-dimensional electron microscopy of single particles, *J. Struct. Biol. 135*, 26−37.
32. Ruiz, T., Kopperschlager, G., and Radermacher, M. (2001) The first three-dimensional structure of phosphofructokinase from *Saccharomyces cerevisiae* determined by electron microscopy of single particles, *J. Struct. Biol. 136*, 167−180.
33. Orlova, E. V., Dube, P., Harris, J. R., Beckman, E., Zemlin, F., Markl, J., and van Heel, M. (1997) Structure of keyhole limpet hemocyanin type 1 (KLH1) at 15 A resolution by electron cryomicroscopy and angular reconstitution, *J. Mol. Biol. 271*, 417−437.
34. van Heel, M., and Harauz, G. (1986) Resolution criteria for three dimensional reconstruction, *Optik 73*, 19−22.
35. Pettersen, E. F., Goddard, T. D., Huang, C. C., Couch, G. S., Greenblatt, D. M., Meng, E. C., and Ferrin, T. E. (2004) UCSF Chimera—a visualization system for exploratory research and analysis, *J. Comput. Chem. 25*, 1605−1612.
36. Sazanov, L. A., and Hinchliffe, P. (2006) Structure of the hydrophilic domain of respiratory complex I from *Thermus thermophilus*, *Science 311*, 1430−1436.
37. Radermacher, M., Ruiz, T., Clason, T., Benjamin, S., Brandt, U., and Zickermann, V. (2006) The three-dimensional structure of complex I from *Yarrowia lipolytica*: A highly dynamic enzyme, *J. Struct. Biol. 154*, 269−279.
38. Kashani-Poor, N., Zwicker, K., Kerscher, S. and Brandt, U. (2001) A central functional role for the 49-kDa subunit within the catalytic core of mitochondrial complex I, *J. Biol. Chem. 276*, 24082−24087.
39. Zickermann, V., Bostina, M., Hunte, C., Ruiz, T., Radermacher, R. and Brandt, U. (2003) Functional implications from an unexpected position of the 49-kDa subunit of NADH:ubiquinone oxidoreductase, *J. Biol. Chem. 278*, 29072−29078.
40. Yano, T., Dunham, W. R., and Ohnishi, T. (2005) Characterization of the delta muH+-sensitive ubisemiquinone species (SQ(Nf)) and the interaction with cluster N2: new insight into the energy-coupled electron transfer in complex I. *Biochemistry 44*, 1744−1754.
41. Covian, R., Gutierrez-Cirlos, E. B., and Trumpower, B. L. (2004) Anti-cooperative oxidation of ubiquinol by the yeast cytochrome bc1 complex, *J. Biol. Chem. 279*, 15040−15049.
42. Covian, R., and Trumpower, B. L. (2005) Rapid electron transfer between monomers when the cytochrome bc1 complex dimer is reduced through center N, *J. Biol. Chem. 280*, 22732−22740.
43. Lange, C., and Hunte, C. (2002) Crystal structure of the yeast cytochrome bc1 complex with its bound substrate cytochrome c, *Proc. Natl. Acad. Sci. U.S.A. 99*, 2800−2805.
44. Pfeiffer, K., Gohil, V., Stuart, R. A., Hunte, C., Brandt, U., Greenberg, M. L., and Schägger, H. (2003) Cardiolipin stabilizes respiratory chain supercomplexes, *J. Biol. Chem. 278*, 52873−52880.
45. Mileykovskaya, E., Zhang, M., and Dowhan, W. (2005) Cardiolipin in energy transducing membranes, *Biochemistry (Moscow) 70*, 154−158.
46. Gong, X., Yu, L., Xia, D., and Yu, C.-A. (2005) Evidence for electron equilibrium between the two hemes bL in the dimeric cytochrome bc1 complex, *J. Biol. Chem. 280*, 9251−9257
47. Radermacher, M., Wagenknecht, T., Grassucci, R., Franck, J., Inui, M., Chadwick, C., and Fleischer, S. (1992) Cryo-EM of the native structure of the calcium release channel/ryanodine receptor from sarcoplasmic reticulum, *Biophys. J. 61*, 936−940.
48. Parcej, D. N., and Eckhardt-Strelau, L. (2003) Structural characterisation of neuronal voltage-sensitive K^+ channels heterologously expressed in *Pichia pastoris*, *J. Mol. Biol. 333*, 103−166.

BI700983H